

Article

Low-Coordinate Dinuclear Dysprosium(III) Single Molecule Magnets Utilizing LiCl as Bridging Moieties and Tris(amido)amine as Blocking Ligands

Maria Brzozowska, Gabriela Handzlik , Mikolaj Zychowicz and Dawid Pinkowicz * 

Faculty of Chemistry, Jagiellonian University, Gronostajowa 2, 30-387 Kraków, Poland; maria.brzozowska@student.uj.edu.pl (M.B.); gabriela.handzlik@uj.edu.pl (G.H.); mikolaj.zychowicz@doctoral.uj.edu.pl (M.Z.)

* Correspondence: dawid.pinkowicz@uj.edu.pl

Abstract: A low-coordinate dinuclear dysprosium complex $\{[\text{Dy}(\text{N}_3\text{N})(\text{THF})][\text{LiCl}(\text{THF})]\}_2$ (**Dy**₂) with a double bridging 'LiCl' moiety and tris(amido)amine (N_3N)^{3−} anions as a blocking ligand is synthesized and characterized structurally and magnetically. Thanks to the use of the chelating blocking ligand (N_3N)^{3−} equipped with large steric $-\text{SiMe}_3$ groups, the coordination sphere of both Dy^{III} ions is restricted to only six donor atoms. The three amido nitrogen atoms determine the orientation of the easy magnetization axes of both Dy^{III} centers. Consequently, **Dy**₂ shows slow magnetic relaxation typical for single molecule magnets (SMMs). However, the effective energy barrier for magnetization reversal determined from the AC magnetic susceptibility measurements is much lower than the separation between the ground and the first excited Kramers doublet based on the CASSCF ab initio calculations. In order to better understand the possible influence of the anticipated intramolecular magnetic interactions in this dinuclear molecule, its Gd^{III}-analog $\{[\text{Gd}(\text{N}_3\text{N})(\text{THF})][\text{LiCl}(\text{THF})]\}_2$ (**Gd**₂) is also synthesized and studied magnetically. Detailed magnetic measurements reveal very weak antiferromagnetic interactions in **Gd**₂. This in turn suggests similar antiferromagnetic interactions in **Dy**₂, which might be responsible for its peculiar SMM behavior and the absence of the magnetic hysteresis loop.

Keywords: nanomagnetism; single molecule magnet; dysprosium; gadolinium; molecular magnetism; lanthanides; slow relaxation of the magnetization



Citation: Brzozowska, M.; Handzlik, G.; Zychowicz, M.; Pinkowicz, D. Low-Coordinate Dinuclear Dysprosium(III) Single Molecule Magnets Utilizing LiCl as Bridging Moieties and Tris(amido)amine as Blocking Ligands. *Magnetochemistry* **2021**, *7*, 125. <https://doi.org/10.3390/magnetochemistry7090125>

Academic Editor: Fabrice Pointillart

Received: 29 July 2021

Accepted: 7 September 2021

Published: 11 September 2021

Publisher's Note: MDPI stays neutral with regard to jurisdictional claims in published maps and institutional affiliations.



Copyright: © 2021 by the authors. Licensee MDPI, Basel, Switzerland. This article is an open access article distributed under the terms and conditions of the Creative Commons Attribution (CC BY) license (<https://creativecommons.org/licenses/by/4.0/>).

1. Introduction

Polynuclear lanthanide (Ln) complexes often exhibit slow magnetic relaxation and related single molecule magnet (SMM) behavior similar to their more famous mononuclear relatives [1–3] but show also the influence of the superexchange interactions. Similarly to mononuclear Ln-SMMs, the field of the polynuclear congeners is also dominated by Dy^{III} [4–8]. Due to very weak intermolecular magnetic interactions between the lanthanide ions in such polynuclear compounds, the slow relaxation of the magnetization is usually dominated by single-ion effects which can be determined by performing experiments involving the diamagnetic dilution of the investigated compounds with Y or La [9]. Obviously, the employment of longer bridging ligands leads to a good separation of the magnetic centers and therefore the possible slow magnetic relaxation becomes a single-ion effect [10]. Due to the weakness of the magnetic interactions in lanthanide-based compounds, only short molecular bridges could provide sufficient communication between the magnetic centers that could influence the slow magnetic relaxation of the compound [3]. Still, the exchange coupling constants between the lanthanide ions in Ln-SMMs, even with very short bridges, are one or two orders of magnitude smaller than the typical values of the energy barrier for the magnetization reversal (J -values are typically in the range 0.1–3 cm^{−1} for diamagnetic bridging ligands). The highest exchange coupling constant for

a polynuclear Ln-SMMs was determined by studying the Gd^{III} congener of the famous [N₂]³⁻ bridged dinuclear Tb-SMM $\{[(\text{Me}_3\text{Si})_2\text{N}]_2(\text{THF})\text{Tb}^{\text{III}}\}_2(\mu\text{-}\eta^2\text{:}\eta^2\text{-N}_2)^-$ [11]. The magnetic interaction between the Gd^{III} and the paramagnetic [N₂]³⁻ molecular bridge was reported to be -27 cm^{-1} ($\hat{H} = -2J\hat{S}_1\hat{S}_2$ Hamiltonian type) [12]. It is noteworthy that in a complex bridged by a radical bipyrimidyl ligand the exchange interaction ($J = -10\text{ cm}^{-1}$; $\hat{H} = -2J\hat{S}_1\hat{S}_2$ Hamiltonian type) [13] was a bit weaker than in the complex bridged by a significantly smaller [N₂]³⁻.

The magnetic interactions between the lanthanide ions can lead to a shift of otherwise-degenerate m_J sublevels to different energies and reduce the probability of the QTM (quantum tunneling of magnetization) [3]. QTM is frequently the reason for a very fast relaxation acceleration under zero magnetic field, so its exclusion is crucial to improve single molecule magnet performance. Even weak exchange interaction (mostly dipolar in nature) between two lanthanide ions can be significant enough to hinder the quantum tunneling of magnetization at $H_{\text{DC}} = 0$ [14–20]. Moreover, magnetic interactions are necessary to engineer universal qubits (quantum gates) as demonstrated for dinuclear LnLn' molecules [21]. Therefore, searching for polynuclear Ln-SMMs with effective magnetic interactions is highly desired.

The design of polynuclear Ln-SMMs is challenging because of the difficulties in predicting how the lanthanides interact with each other and what would be the orientation of their easy magnetization axes in a particular chemical and geometrical environment [22]. The task becomes even more difficult when very small ligands, such as NO₃⁻, H₂O, OH⁻, THF, etc., are allowed to coordinate to the metal centers leading to complexes with high coordination numbers ≥ 8 and uncontrolled coordination geometries. This is why we have focused our efforts on obtaining Ln complexes with a bulky chelating ligand tris(N-trimethylsilyl-2-amidoethyl)amine (N₃N)³⁻ in the form of a lithium salt [23]. The (N₃N)³⁻ ligand was successfully used to obtain transition metal complexes with a strictly controlled coordination geometry such as (N₃N)Mo^{IV}Cl [24] showing extremely attractive chemical properties such as N₂ activation or a family of [M^{II}(N₃N)Li(THF)] (M=Mn, Fe, Co, Ni) compounds with a significant magnetic anisotropy associated with their trigonal pyramidal geometry imposed by the (N₃N)³⁻ ligand [25].

Herein, we describe a dinuclear SMM based on Dy^{III} $\{[\text{Dy}(\text{N}_3\text{N})(\text{THF})][\text{LiCl}(\text{THF})]\}_2$ (**Dy**₂) and its Gd^{III} analog (**Gd**₂). Both compounds are obtained by reacting the aforementioned lithium salt of the tris(amido)amine with the respective anhydrous LnCl₃ salts (Ln = Dy, Gd) in THF. Interestingly, the bridge between the two lanthanide ions consists of two Cl⁻ anions and two Li⁺ cations stabilized by two THF molecules. The influence of the bridging LiCl on the magnetic properties of both **Dy**₂ and **Gd**₂ is discussed in light of the CASSCF calculations.

2. Results and Discussion

2.1. Synthesis and Crystal Structure

Both dinuclear compounds $\{[\text{Dy}(\text{N}_3\text{N})(\text{THF})][\text{LiCl}(\text{THF})]\}_2$ (**Dy**₂) and $\{[\text{Gd}(\text{N}_3\text{N})(\text{THF})][\text{LiCl}(\text{THF})]\}_2$ (**Gd**₂) (N₃N = tris(N-trimethylsilyl-2-amidoethyl)amine; $[(\text{Me}_3\text{SiNCH}_2\text{CH}_2)_3\text{N}]^{3-}$; Figure 1a) were obtained by reacting the respective anhydrous chlorides with Li₃(N₃N) in anhydrous THF followed by solvent removal and extraction with pentane. Noteworthy, the **Gd**₂ and **Dy**₂ presented in this work are formed under very similar reaction conditions to the monometallic Er^{III} complex reported by us recently [26].

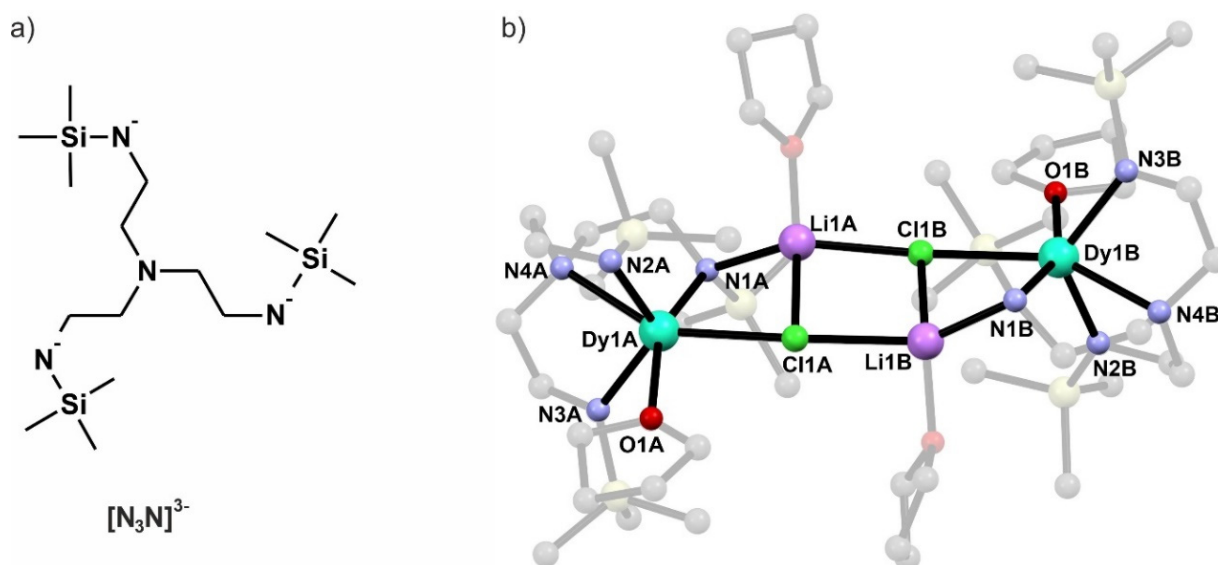


Figure 1. Structural formula of the trianionic tris(*N*-trimethylsilyl-2-amidoethyl)amine ligand (a) and the crystal structure of $\{[\text{Dy}(\text{N}_3\text{N})(\text{THF})][\text{LiCl}(\text{THF})]\}_2$ (**Dy**₂) (b) with atom labeling scheme (the blocking ligands $(\text{N}_3\text{N})^{3-}$, THF molecules and hydrogen atoms are dimmed for the sake of clarity).

Crystals of **Dy**₂ and **Gd**₂ are grown from pentane solutions at $-40\text{ }^\circ\text{C}$. They crystallize in a triclinic system, space group $P2_1/c$ as determined by single crystal X-ray diffraction (SCXRD) structural analysis. Both compounds are isostructural and therefore **Dy**₂ will be discussed as the representative one. Selected crystallographic details are presented in Table 1. The asymmetric unit contains the whole molecule consisting of two metal centers blocked by $(\text{N}_3\text{N})^{3-}$ ligand and connected by double LiCl bridge with THF attached to it (Figure 1b). Both lanthanide centers within the molecule are coordinated by four nitrogen atoms of the $(\text{N}_3\text{N})^{3-}$ ligands, one chloride and one oxygen atom of the THF molecule leading to a pseudo-octahedral coordination geometry of both centers. The chelating $(\text{N}_3\text{N})^{3-}$ ligands do not block all of the coordination sites, unlike in many transition metal complexes [24,25], but leave enough space for the ‘LiCl’ bridge and coordinated THF molecule. The distance between the two lanthanides is 7.937 Å for **Dy**₂ and 7.961 Å for **Gd**₂. Such a long distance suggests that the intramolecular magnetic interactions between the two metal centers within the dinuclear ‘units’ should be very weak. Intermolecular Ln...Ln distances are also long (the shortest ones are 7.969 Å for **Dy**₂ and 8.122 Å for **Gd**₂). Figure 2 presents the packing diagram of the Dy(LiCl)₂Dy cores with the shortest intermolecular distances highlighted as a dotted line. As aforementioned, the coordination spheres of the lanthanide ions in **Dy**₂ and **Gd**₂ are six-coordinate and resemble a strongly distorted octahedron. Table 2 provides the metric parameters of the first coordination spheres in both compounds. The distortion from the octahedral geometry is caused mainly by significantly elongated Ln-Cl bonds: 2.733(1) Å, 2.740(1) Å for **Dy**₂ and 2.763(1) Å, 2.769(1) Å for **Gd**₂ as compared to the average 2.38(11) Å for **Dy**₂ and 2.41(11) Å for **Gd**₂. The angles presented in Table 2 also clearly show how strongly the coordination spheres of the metal centers in both compounds are distorted from the ideal six-coordinate octahedral geometry.

Table 1. Selected crystallographic parameters for Dy_2 and Gd_2 .

	$\{\{\text{Dy}(\text{N}_3\text{N})(\text{THF})\}[\text{LiCl}(\text{THF})]\}_2$ (Dy_2)	$\{\{\text{Gd}(\text{N}_3\text{N})(\text{THF})\}[\text{LiCl}(\text{THF})]\}_2$ (Gd_2)
CCDC deposition number	2099063	2099064
Instrument	Bruker D8 Quest Eco, Photon II CPAD	
Radiation	Mo $\text{K}\alpha$ ($\lambda = 0.71073 \text{ \AA}$)	
Formula	$\text{C}_{46}\text{H}_{110}\text{Cl}_2\text{Dy}_2\text{Li}_2\text{N}_8\text{O}_4\text{Si}_6$	$\text{C}_{23}\text{H}_{55}\text{ClGdLiN}_4\text{O}_2\text{Si}_3$
$M_r/\text{g mol}^{-1}$	1417.73	703.62
T/K	100 (2)	100 (2)
Crystal system	monoclinic	monoclinic
Space group	$P 2_1/c$	$P 2_1/c$
$a/\text{\AA}$	27.597 (2)	27.664 (2)
$b/\text{\AA}$	18.9742 (14)	19.0319 (14)
$c/\text{\AA}$	12.9329 (10)	12.9766 (10)
$\alpha/^\circ$	90	90
$\beta/^\circ$	95.962 (2)	96.151 (2)
$\gamma/^\circ$	90	90
$V/\text{\AA}^3$	6735.4 (9)	6792.8 (9)
Z	4	4
$\rho_{\text{calc}}/\text{g}\cdot\text{cm}^{-3}$	1.398	1.376
μ/mm^{-1}	2.429	2.161
F(000)	2920	2904
Crystal size/ mm^3	0.37 0.31 0.23	0.27 0.25 0.17
2θ range/ $^\circ$	1.91–27.88	2.31–27.92
Completeness/%	98.4	99.6
Reflections collected	70,952	77,170
Independent reflections	15,811	16,200
R_{int}	0.0617	0.0898
Parameters/restraints	649/18	649/18
$R[F_o > 2\sigma(F_o)]$	0.0355	0.0498
$wR(F^2)$	0.0840	0.0822
GOF on F^2	1.040	1.049
$\Delta\rho_{\text{max}}, \Delta\rho_{\text{min}}/\text{e}\cdot\text{\AA}^{-3}$	0.973/−0.802	1.410/−1.579

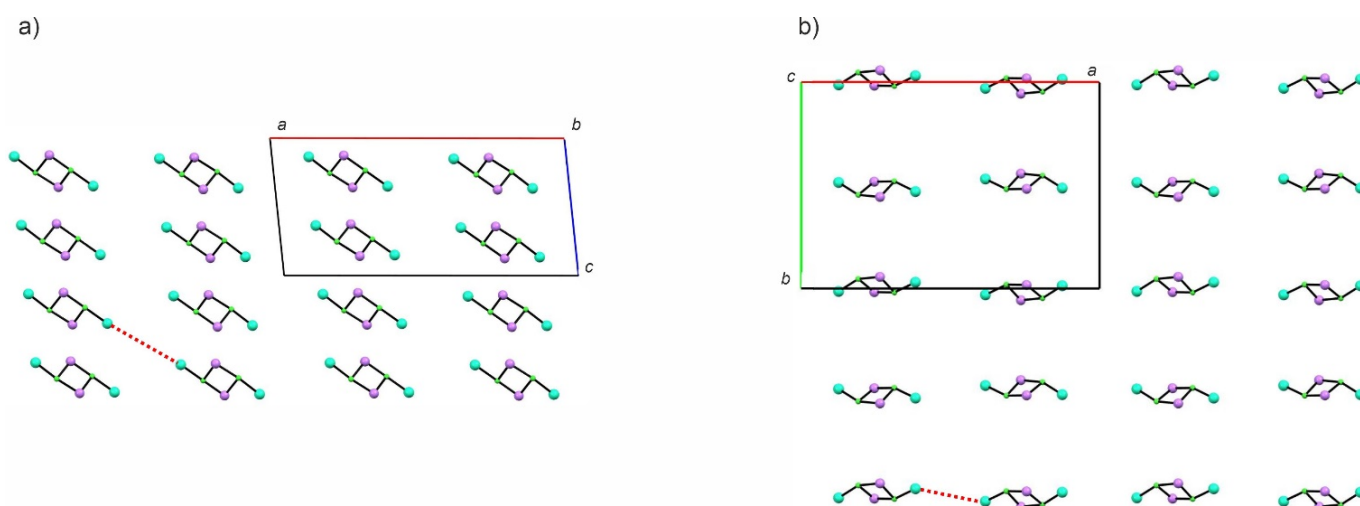
**Figure 2.** Structural packing diagram for Dy_2 presented along the b (a) and c (b) crystallographic direction. The red dotted lines indicate the shortest intermolecular $\text{Dy}\cdots\text{Dy}$ distances.

Table 2. Selected bond lengths and angles of the coordination spheres of Dy in **Dy**₂ and Gd in **Gd**₂.

	{[Dy(N ₃ N)(THF)][LiCl(THF)] ₂ (Dy ₂)}		{[Gd(N ₃ N)(THF)][LiCl(THF)] ₂ (Gd ₂)}	
	x = A	x = B	x = A	x = B
M1x-O1x	2.461 (3)	2.494 (3)	2.488 (4)	2.518 (4)
M1x-N1x	2.385 (3)	2.380 (3)	2.415 (4)	2.411 (4)
M1x-N2x	2.271 (3)	2.263 (3)	2.298 (4)	2.292 (4)
M1x-N3x	2.273 (4)	2.291 (4)	2.306 (4)	2.318 (4)
M1x-N4x	2.508 (3)	2.519 (4)	2.544 (4)	2.547 (4)
M1x-Cl1x	2.733 (1)	2.740 (1)	2.763 (1)	2.769 (1)
N1x-M1x-N4x	74.06 (11)	73.41 (12)	73.31 (14)	72.83 (14)
N2x-M1x-N4x	72.69 (12)	73.14 (13)	72.20 (14)	72.41 (15)
N3x-M1x-N4x	72.40 (12)	72.56 (12)	71.10 (15)	71.66 (15)
O1x-M1x-N4x	129.35 (10)	127.14 (11)	129.65 (13)	127.28 (13)
Cl1x-M1x-N4x	149.13 (7)	150.45 (7)	148.44 (8)	149.97 (9)
N1x-M1x-Cl1x	79.02 (9)	81.92 (9)	78.96 (10)	81.93 (11)
N2x-M1x-Cl1x	127.46 (9)	127.68 (10)	128.16 (11)	128.48 (12)
N3x-M1x-Cl1x	104.87 (9)	103.83 (9)	106.31 (11)	104.88 (11)
O1x-M1x-Cl1x	79.34 (7)	79.92 (7)	79.67 (9)	80.23 (9)
N1x-M1x-N2x	99.68 (12)	98.94 (13)	99.63 (15)	98.43 (16)
N2x-M1x-O1x	85.68 (11)	83.24 (11)	86.48 (14)	84.19 (14)
O1x-M1x-N3x	83.28 (11)	82.41 (11)	83.60 (14)	82.49 (14)
N3x-M1x-N1x	111.98 (12)	113.46 (13)	111.21 (15)	112.96 (15)

2.2. DC Magnetic Properties

The direct-current (DC) magnetic properties of **Dy**₂ and **Gd**₂ in the form of $\chi T(T)$ (χ —molar magnetic susceptibility) and $M(H)$ (M —molar magnetization, H —magnetic field strength) are presented in Figure 3. **Gd**₂ shows magnetic properties typical for a completely isotropic magnetic system composed of two Gd^{III} ions with a constant χT value of 16.0 cm³·K·mol⁻¹ down to the lowest temperatures where only a slight decrease occurs due to the Zeeman effect and the antiferromagnetic Gd^{III}·Gd interactions. $M(H)$ curve reaches the saturation value of 13.9 μ_B already at ca. 55 kOe and remains constant up to 70 kOe. Both experimental curves (black points and blue circles in Figure 3) match well the best fit with $g_{Gd} = 2.00$ (1) and $J_{GdGd} = -0.004$ (1) cm⁻¹ (PHI software [27]). **Dy**₂, on the other hand, shows a gradual decrease of the $\chi T(T)$ related to the thermal depopulation of the m_j states. The room temperature χT value of 27.7 cm³·K·mol⁻¹ corresponds well with the expected 28.34 cm³·K·mol⁻¹ for two isolated Dy^{III} ions (⁶H_{15/2}, $g_J = 4/3$) [28]. Both experimental dependences $\chi T(T)$ and $M(H)$ for **Dy**₂ (black points and red circles, respectively, in Figure 3) are well reproduced by the CASSCF calculations (red solid lines in Figure 3; for details see section Ab initio calculations) which confirm the significant magnetic anisotropy of **Dy**₂. A very steep decrease of the χT at around 1.8 K, which is not reproduced by the CASSCF calculations (red line in Figure 3a), suggests non-negligible antiferromagnetic superexchange coupling between Dy^{III} ions in **Dy**₂, most probably of intramolecular character rather than intermolecular. Intermolecular magnetic coupling in the case of **Dy**₂ should have a through-space dipole–dipole character due to the absence of other intermolecular contacts between the neighboring **Dy**₂ molecules—except the van der Waals contacts. Such contacts usually yield much weaker magnetic coupling than the superexchange even through several atoms as in the case of the double LiCl bridge within the **Dy**₂ dimer.

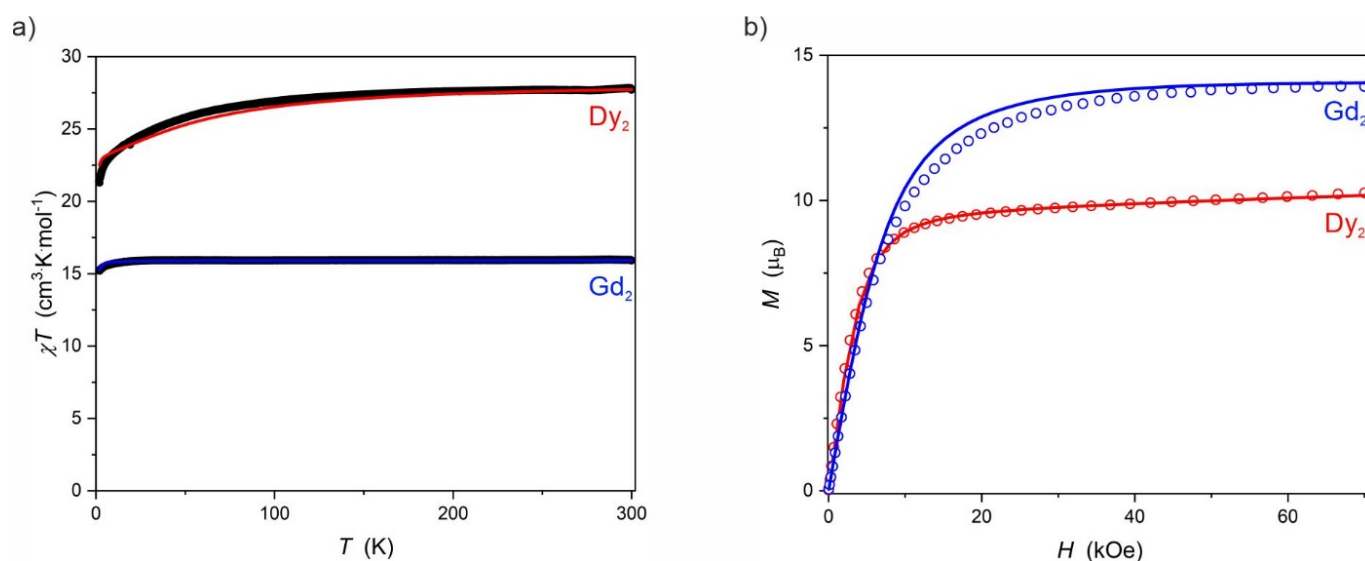


Figure 3. $\chi T(T)$ recorded at 1000 Oe (a) and $M(H)$ recorded at 2.0 K (b) for Dy_2 (red) and Gd_2 (blue). Black overlapping points in (a) represent the experimental data and the colored solid lines correspond to the CASSCF ab initio calculations (for details see below) in the case of Dy_2 and the best fit (PHI software) in the case of Gd_2 with $g = 2.00$ and $J_{\text{GdGd}} = -0.004$ (1).

2.3. AC Magnetic Properties

Alternating-current (AC) magnetic susceptibility (χ) measurements revealed slow magnetic relaxation for Dy_2 under an applied DC field. The frequency (ν) dependence in the 1–1000 Hz range under varied magnetic fields 100–7000 Oe recorded at 3.5 K is presented in Figure 4. In the 200–3000 Oe DC field, only one major maximum can be observed in the out-of-phase magnetic susceptibility (χ''). Only under DC fields larger than 3000 Oe a second maximum reveals itself at lower frequency range, which was not analyzed. The main maximum shifts from around 15 Hz at $H_{\text{DC}} = 200$ Oe to around 7 Hz at the magnetic field in the 800–1400 Oe range and then shifts towards higher frequencies under $H_{\text{DC}} > 2000$ Oe.

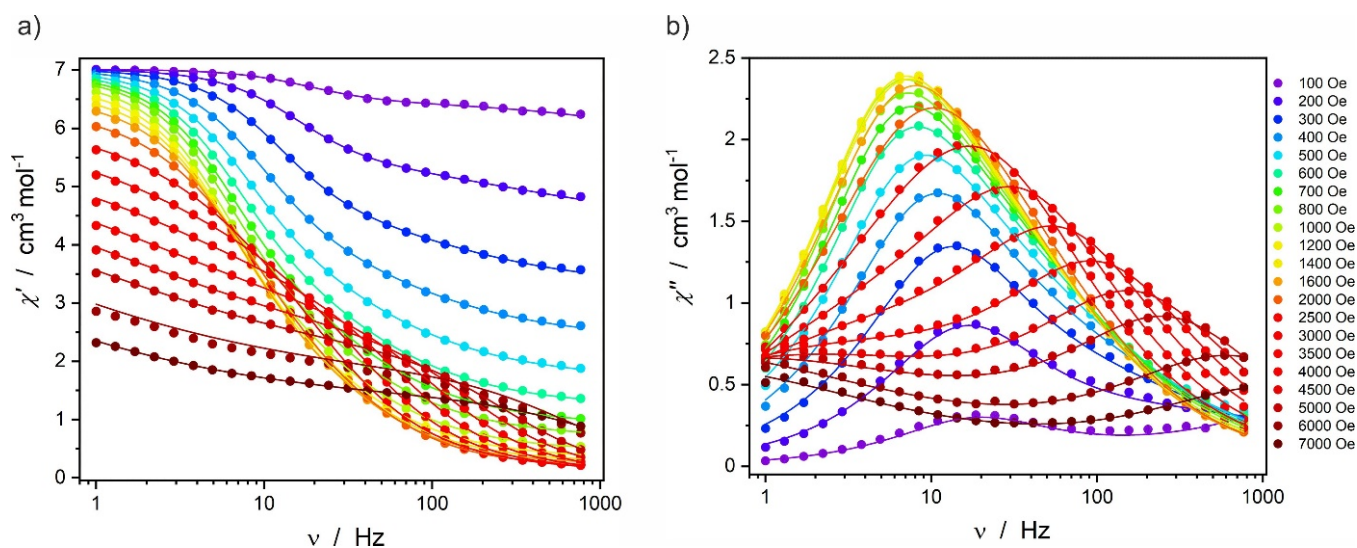


Figure 4. In-phase χ' (a) and out-of-phase χ'' (b) AC magnetic susceptibility for Dy_2 recorded at 3.5 K under various magnetic fields H_{DC} in the 100–7000 Oe range.

The AC magnetic susceptibility was then studied under the optimal magnetic field of 1000 Oe at various temperatures in the 2.8–8.3 K range (Figure 5). The maxima in the $\chi''(\nu)$ plots show a clear shift towards higher frequencies when the temperature is increased.

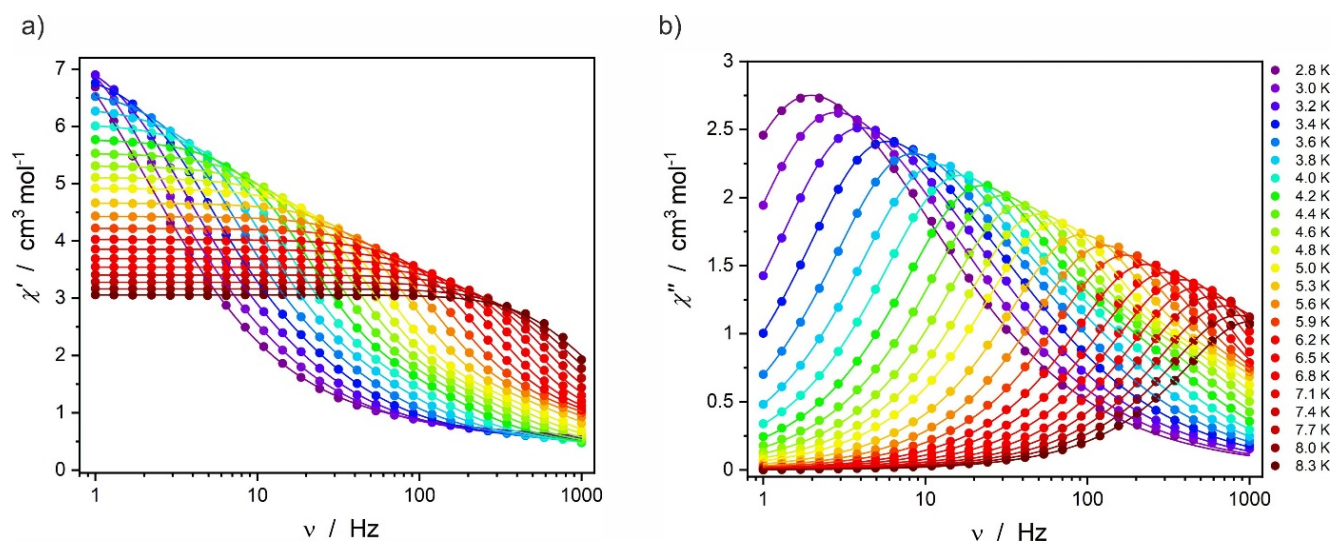


Figure 5. In-phase χ' (a) and out-of-phase χ'' (b) AC magnetic susceptibility for Dy_2 recorded under 1000 Oe magnetic field at various temperatures in the 2.8–8.3 K range.

The AC data presented in Figures 4 and 5 were fitted using a modified Debye model [29] and the resulting best fits are shown in the respective Figures as colored solid lines. The extracted relaxation times of the magnetization were then plotted vs. the magnetic field $\tau^{-1}(H)$ (Figure 6a) and vs. the temperature $\ln\tau(T^{-1})$ (Figure 6b). Equation (1) was used to fit the magnetic field dependence of the relaxation times τ extracted from the $\chi', \chi''(\nu)$ under various magnetic fields [30]:

$$\tau^{-1}(H) = A_1 / (1 + A_2 H^2) + A_3 H^4 + A_4 \quad (1)$$

where the first part is the quantum tunneling of magnetization (QTM), the second one is related to the direct relaxation process and the constant value A_4 stands for the contribution of the field-independent processes (Orbach and Raman) (Figure 6). The best fit parameters are gathered in Table 3 (top part).

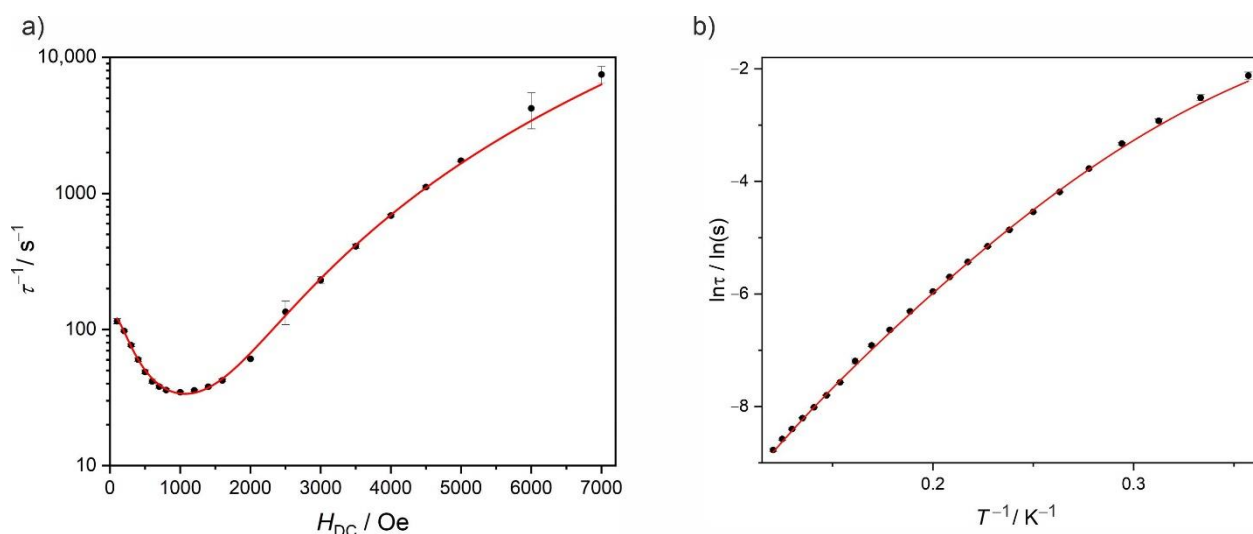


Figure 6. Field dependence of τ^{-1} at 3.5 K in the 100–7000 Oe range (a) and temperature dependence of $\ln\tau$ under 1000 Oe in the 2.8–8.3 K range (b) for Dy_2 . Red solid lines are the best fits to Equation (1) (a) or Equation (2) (b) (for details see text).

Table 3. Best fit parameters obtained by fitting $\tau^{-1}(H)$ (Figure 6a) and $\ln\tau(T^{-1})$ (Figure 6b) to Equations (1) and (2), respectively.

T/K	3.5 K	
range/Hz	1–1000	
field range/Oe	100–7000	
A_1/s^{-1}	110 (7)	field dependence (Figure 6a)
A_2/Oe^{-2}	$1.2 (2) \cdot 10^{-5}$	
A_3/Oe^{-4}	$2.63 (5) \cdot 10^{-12}$	
A_4/s^{-1}	22.9 (9)	
R^2	0.995	
H_{DC}/Oe	1000	
range/Hz	1–1000	
temp. range/K	2.8–8.3	
C_0/s^{-1}	0 (fixed)	temperature dependence (Figure 6b)
$C_1/s^{-1}K^{-1}$	0.75 (fixed)	
$C_2/s^{-1}K^{-n}$	0.015 (7)	
n	5.81 (33)	
τ_0/s	$4.9 (1.9) \cdot 10^{-6}$	
$(U_{eff}/k_B)/K$	34 (2)	
R^2	0.99956	

The values of the relaxation time τ extracted from the temperature dependence of the $\chi', \chi''(\nu)$ were fitted using Equation (2) [30]:

$$\ln\tau(T^{-1}) = \ln[(C_0 + C_1T + C_2T^n + \tau_0^{-1}\exp(-U_{eff}/k_B T))^{-1}] \quad (2)$$

where the constant value C_0 stands for the temperature-independent QTM, the second part is related to the direct process, C_2 and n describe the Raman process and the last part characterizes the contribution of the Orbach relaxation. The best fit parameters are gathered in Table 3 (bottom part). The QTM contribution under the applied magnetic field of 1000 Oe was fixed to zero in this equation, as the analysis of the field dependence of τ did not show significant contribution of QTM process under this optimal applied DC magnetic field. The contribution of the direct process was calculated from Equation (1) and then inserted into Equation (2) as a fixed value ($C_1 = 0.75 \text{ s}^{-1} \cdot \text{K}^{-1}$) (Figure 6b).

The fit of the temperature dependence of $\ln\tau$ shows a significant contribution of the Raman relaxation process ($C_2 = 0.015 (7) \text{ s}^{-1} \cdot \text{K}^{-n}$, $n = 5.81 (33)$) and a small contribution of the Orbach process, especially visible at lower temperatures ($\tau_0 = 4.9 (1.9) \cdot 10^{-6} \text{ s}$ and $U_{eff}/k_B = 34 (2) \text{ K}$ or 23.6 cm^{-1} which might be significantly underestimated).

2.4. Ab Initio Calculations

Theoretical calculations CASSCF were performed separately for both Dy^{III} centers based on the SCXRD structural models using the OpenMolcas software [31] (for details, see Table S1 in the Supplementary Materials; SM). The ground state Kramers doublet (KD) for both centers is composed mainly of the $|\pm 15/2 \rangle m_J$ state with a significantly axial character (Tables S2 and S3 in the SM) and nearly parallel easy magnetization axes (Figure 7a). The first excited KD doublet is located ca. 130 cm^{-1} above the ground KD, which is significantly larger than the experimentally estimated energy barrier for the magnetization reversal $U_{eff} = 23.6 \text{ cm}^{-1}$ (Figure 7b) This suggests that the relaxation of the magnetization in Dy_2 is controlled by the Raman relaxation mechanism (not Orbach), as already pointed out in the section discussing the AC magnetic data.

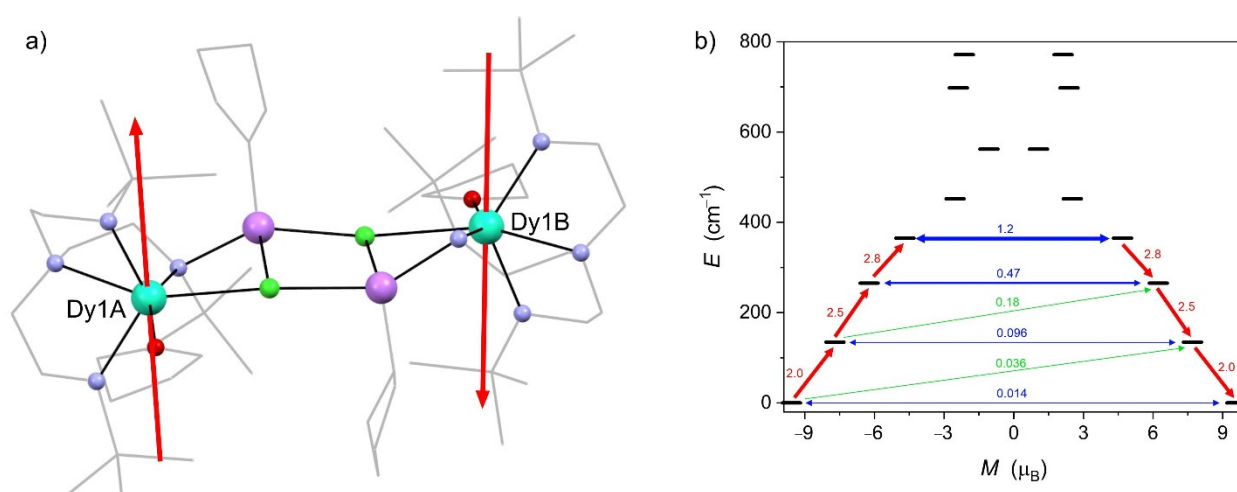


Figure 7. Structural diagram of Dy_2 with the red sticks indicating the orientation of the easy magnetization axes of the ground state Kramers doublet (KD) for both Dy^{III} centers obtained from the CASSCF calculations (the direction indicated by the arrows is hypothetical, assuming intramolecular antiferromagnetic interactions between the Dy^{III} centers within the dimer based on the analysis of the DC magnetic properties of Dy_2 and its Gd_2 analogue) (a). Energy diagram of the calculated Kramers doublets within the ${}^6\text{H}_{15/2}$ multiplet of one of the Dy^{III} centers in Dy_2 (b). Arrows correspond to the most important magnetization relaxation pathways.

3. Materials and Methods

3.1. General Considerations

The syntheses of the reported compounds as well as their preparation for measurements were performed inside the Inert PureLab HE glovebox filled with argon gas due to their sensitivity to air (predominantly moisture). Solvents (HPLC grade) were passed through the Inert PureSolv EN7 solvent purification system under inert atmosphere. Anhydrous DyCl_3 (99.99%) was purchased from Sigma Aldrich and GdCl_3 (99.9%) was purchased from Alfa Aesar. Both chemicals were used without further purification. $\text{Li}_3(\text{N}_3\text{N})$ was prepared according to the previously published method [23].

3.2. Preparation of Dy_2

Solid DyCl_3 (0.68 mmol, 183 mg) was added in portions into the solution of $\text{Li}_3(\text{N}_3\text{N})$ (0.71 mmol, 272 mg) in 5.90 g of anhydrous THF. The reaction mixture was stirred for 4 days and then the solvent was removed under vacuum and replaced with pentane. The off-white suspension was stirred for 20 min and then filtered using a P4 fritted funnel (gravitational filtering). The solid was extracted with three more portions of pentane. The yellow filtrates were combined and left at $-40\text{ }^\circ\text{C}$ for crystallization. After 3 days colorless crystals were collected. Yield: 70 mg (15%). The identity and purity of the compound was confirmed by powder X-ray diffraction (PXRD) measurements (Figure 8).

3.3. Preparation of Gd_2

Solid GdCl_3 (0.67 mmol, 178 mg) was added in portions into the solution of $\text{Li}_3(\text{N}_3\text{N})$ (0.70 mmol, 267 mg) in 5.90 g of anhydrous THF. The reaction mixture was stirred for 3 h and then the solvent was removed under vacuum and replaced with pentane. The suspension was filtered (P4 fritted funnel; gravitational filtering) and the solid was extracted with three more portions of pentane. The yellowish filtrates were combined and left in the freezer at $-40\text{ }^\circ\text{C}$ for crystallization. After 3 days colorless crystals were collected. Yield: 70 mg (15%). The identity and purity of the compound was confirmed by powder X-ray diffraction (PXRD) measurements (Figure 8, dark blue and light blue solid lines).

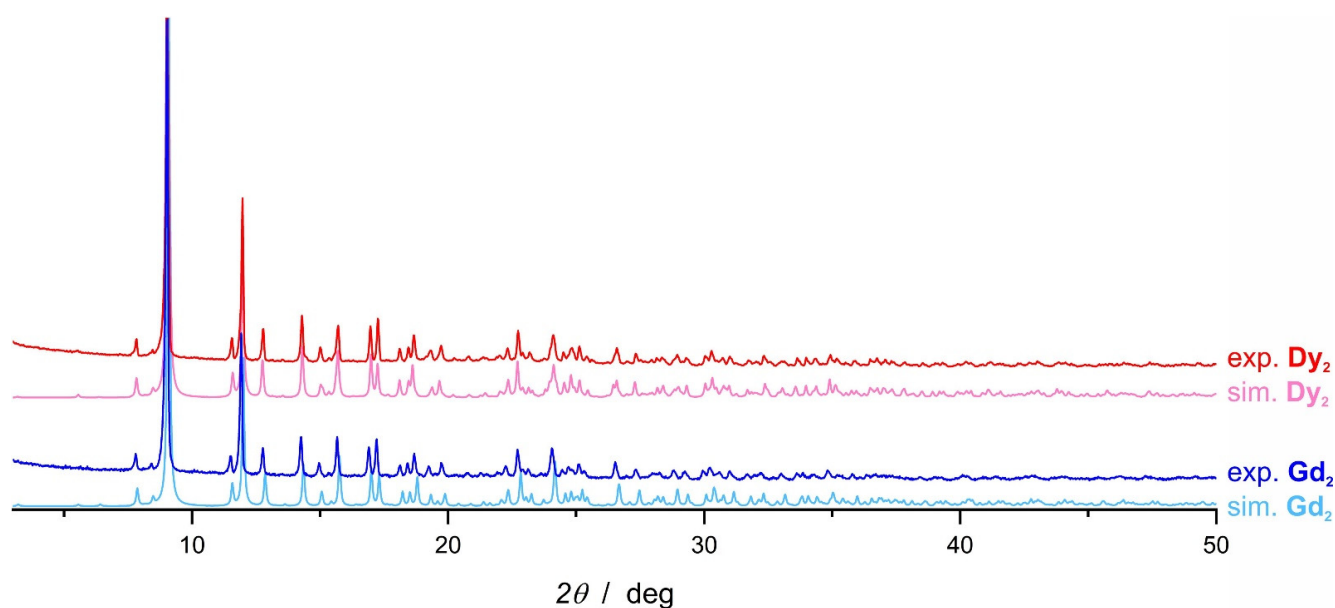


Figure 8. Powder X-ray diffraction patterns: Dy_2 experimental at room temperature (red); Dy_2 simulated from SCXRD data collected at 296 K (pink); Gd_2 experimental at room temperature (blue); Gd_2 simulated from SCXRD data collected at 296 K (bright blue).

3.4. Single Crystal X-ray Diffraction

Data collection was performed using Bruker D8 Quest Eco (Photon50) diffractometer (Mo $K\alpha$ radiation source: sealed tube with Triumph[®] monochromator). The crystals were transferred from the mother liquor directly into the Paratone-N oil and mounted using MiTeGen cryomounts. The data for each compound were collected first at 100 K (complete data for publication) and then at room temperature (296 K; fast data collection for comparison with experimental PXRD patterns). Data processing was performed using Apex3 suite of programs. The structures were solved using direct methods and refined anisotropically (weighted full-matrix least-squares on F^2 [32]). Hydrogen atoms were placed in the calculated positions and refined as riding on the parent atoms. Structural diagrams were prepared using Mercury software. CCDC 2099063 (Dy_2 at 100 K), 2107188 (Dy_2 at 296 K), 2099064 (Gd_2 at 100 K) and 2107189 (Gd_2 at 296 K) contain the supplementary crystallographic data for this paper, which can be obtained free of charge from the Cambridge Crystallographic Data Centre via www.ccdc.cam.ac.uk/data_request/cif (accessed on 2 September 2021). The cif files can also be found in the Supplementary Materials.

3.5. Powder X-ray Diffraction

PXRD measurements were performed at room temperature using Bruker D8 Advance Eco diffractometer equipped with the $\text{CuK}\alpha$ radiation source (sealed tube), the Lynxeye silicon strip detector and a capillary stage. The samples were ground using the agate mortar inside the glovebox and loaded into 0.7 mm glass capillaries.

3.6. Magnetic Measurements

Magnetic measurements were performed using a Quantum Design MPMS-3 magnetometer in the -7 to 7 T magnetic field range and in the 1.8 – 300 K temperature range. The samples were prepared inside the glovebox due to their sensitivity to air. We loaded 25 – 30 mg of each compound into a custom-made Delrin sample holder [33] and sealed it. The experimental data were corrected for the diamagnetism of the sample and the contribution of the sample holder.

4. Conclusions

A new dinuclear dysprosium(III) single molecule magnet comprising six-coordinate Dy^{III} centers shows slow relaxation of the magnetization controlled mainly by QTM at zero applied magnetic field and by Raman relaxation process at $H_{DC} > 0$. The lack of the SMM behavior at zero field is most probably caused by the intramolecular antiferromagnetic interactions transmitted through a double LiCl bridge (similar antiferromagnetic interactions were found for the gadolinium(III) analog of **Dy**₂). The field-induced SMM behavior, on the other hand, is controlled mainly by the Raman relaxation. This is partly confirmed by the CASSCF calculations, which indicate that **Dy**₂ should be a much better-performing SMM than it is actually observed with effective energy barrier for magnetization reversal exceeding 130 cm⁻¹. Further studies involving the diamagnetic dilution of the dinuclear **Dy**₂ with yttrium(III) that would switch off the possible antiferromagnetic interactions are necessary for the complete understanding of the slow relaxation of the magnetization in this compound.

Supplementary Materials: The following are available online at <https://www.mdpi.com/article/10.3390/magnetochemistry7090125/s1>, Table S1: Description and contractions of the basis sets (two models: **S**—smaller, **L**—larger) employed in *ab initio* calculations of the Dy^{III} crystal field, Table S2: Summary of the energy splitting of the ⁶H_{15/2} multiplet of the Dy1A in models: **L**, **S** with pseudo-g-tensors of each Kramers doublet and composition in the $|m_J\rangle$ basis of ground state, Table S3: Summary of the energy splitting of the ⁶H_{15/2} multiplet of the Dy1B in models: **L**, **S** with pseudo-g-tensors of each Kramers doublet and composition in the $|m_J\rangle$ basis of ground state.

Author Contributions: Conceptualization, D.P.; methodology, D.P.; investigation, M.B. and G.H.; resources, D.P.; writing—original draft preparation, G.H. and M.B.; writing—review and editing, D.P.; visualization, D.P., M.B. and G.H.; supervision, D.P.; project administration, D.P.; funding acquisition, D.P.; calculations, M.Z. All authors have read and agreed to the published version of the manuscript.

Funding: This work was funded by the National Science Center within the Sonata Bis project no. 2016/22/E/ST5/00055.

Data Availability Statement: CCDC 2099063 (**Dy**₂ at 100 K), 2107188 (**Dy**₂ at 296 K), 2099064 (**Gd**₂ at 100 K) and 2107189 (**Gd**₂ at 296 K) contain the supplementary crystallographic data for this paper, which can be obtained free of charge from the Cambridge Crystallographic Data Centre via www.ccdc.cam.ac.uk/data_request/cif.

Conflicts of Interest: The authors declare no conflict of interest.

References

1. Goodwin, C.A.P.; Ortu, F.; Reta, D.; Chilton, N.F.; Mills, D.P. Molecular magnetic hysteresis at 60 kelvin in dysprosocenium. *Nature* **2017**, *548*, 439–442. [[CrossRef](#)] [[PubMed](#)]
2. Canaj, A.B.; Dey, S.; Wilson, C.; Céspedes, O.; Rajaraman, G.; Murrie, M. Engineering macrocyclic high performance pentagonal bipyramidal Dy(III) single-ion magnets. *Chem. Commun.* **2020**, *56*, 12037–12040. [[CrossRef](#)]
3. Wang, J.; Li, Q.-W.; Wu, S.-G.; Chen, Y.-C.; Wan, R.-C.; Huang, G.-Z.; Liu, Y.; Liu, J.-L.; Reta, D.; Giansiracusa, M.J.; et al. Opening Magnetic Hysteresis by Axial Ferromagnetic Coupling: From Mono-Decker to Double-Decker Metallocrown. *Angew. Chem. Int. Ed.* **2021**, *60*, 5299–5306. [[CrossRef](#)]
4. Habib, F.; Murugesu, M. Lessons learned from dinuclear lanthanide nano-magnets. *Chem. Soc. Rev.* **2013**, *42*, 3278–3288. [[CrossRef](#)] [[PubMed](#)]
5. Woodruff, D.N.; Winpenny, R.E.P.; Layfield, R.A. Lanthanide Single-Molecule Magnets. *Chem. Rev.* **2013**, *113*, 5110–5148. [[CrossRef](#)]
6. Xin, Y.; Wang, J.; Zychowicz, M.; Zakrzewski, J.J.; Nakabayashi, K.; Sieklucka, B.; Chorazy, S.; Ohkoshi, S.-I. Dehydration–Hydration Switching of Single-Molecule Magnet Behavior and Visible Photoluminescence in a Cyanido-Bridged DyIII/CoIII Framework. *J. Am. Chem. Soc.* **2019**, *141*, 18211–18220. [[CrossRef](#)]
7. Li, X.-L.; Wu, J.; Tang, J.; Le Guennic, B.; Shi, W.; Cheng, P. A planar triangular Dy₃ + Dy₃ single-molecule magnet with a toroidal magnetic moment. *Chem. Commun.* **2016**, *52*, 9570–9573. [[CrossRef](#)]
8. Hewitt, I.J.; Tang, J.; Madhu, N.T.; Anson, C.E.; Lan, Y.; Luzon, J.; Etienne, M.; Sessoli, R.; Powell, A.K. Coupling Dy₃ Triangles Enhances Their Slow Magnetic Relaxation. *Angew. Chem. Int. Ed.* **2010**, *49*, 6352–6356. [[CrossRef](#)]
9. Habib, F.; Lin, P.-H.; Long, J.; Korobkov, I.; Wernsdorfer, W.; Murugesu, M. The Use of Magnetic Dilution To Elucidate the Slow Magnetic Relaxation Effects of a Dy₂ Single-Molecule Magnet. *J. Am. Chem. Soc.* **2011**, *133*, 8830–8833. [[CrossRef](#)] [[PubMed](#)]

10. Habib, F.; Long, J.; Lin, P.-H.; Korobkov, I.; Ungur, L.; Wernsdorfer, W.; Chibotaru, L.F.; Murugesu, M. Supramolecular architectures for controlling slow magnetic relaxation in field-induced single-molecule magnets. *Chem. Sci.* **2012**, *3*, 2158–2164. [[CrossRef](#)]
11. Rinehart, J.D.; Fang, M.; Evans, W.J.; Long, J.R. A N_2^{3-} Radical-Bridged Terbium Complex Exhibiting Magnetic Hysteresis at 14 K. *J. Am. Chem. Soc.* **2011**, *133*, 14236–14239. [[CrossRef](#)]
12. Rinehart, J.D.; Fang, M.; Evans, W.J.; Long, J.R. Strong exchange and magnetic blocking in N_2^{3-} -radical-bridged lanthanide complexes. *Nat. Chem.* **2011**, *3*, 538–542. [[CrossRef](#)] [[PubMed](#)]
13. Demir, S.; Zadrozny, J.M.; Nippe, M.; Long, J.R. Exchange Coupling and Magnetic Blocking in Bipyrimidyl Radical-Bridged Lanthanide Complexes. *J. Am. Chem. Soc.* **2012**, *134*, 18546–18549. [[CrossRef](#)] [[PubMed](#)]
14. Lin, P.-H.; Sun, W.-B.; Yu, M.-F.; Li, G.-M.; Yan, P.-F.; Murugesu, M. An unsymmetrical coordination environment leading to two slow relaxation modes in a Dy₂ single-molecule magnet. *Chem. Commun.* **2011**, *47*, 10993–10995. [[CrossRef](#)] [[PubMed](#)]
15. Guo, Y.-N.; Xu, G.-F.; Wernsdorfer, W.; Ungur, L.; Guo, Y.; Tang, J.; Zhang, H.-J.; Chibotaru, L.F.; Powell, A.K. Strong Axiality and Ising Exchange Interaction Suppress Zero-Field Tunneling of Magnetization of an Asymmetric Dy₂ Single-Molecule Magnet. *J. Am. Chem. Soc.* **2011**, *133*, 11948–11951. [[CrossRef](#)] [[PubMed](#)]
16. Sakaue, S.; Fuyuhira, A.; Fukuda, T.; Ishikawa, N. Dinuclear single-molecule magnets with porphyrin–phthalocyanine mixed triple-decker ligand systems giving SAP and SP coordination polyhedra. *Chem. Commun.* **2012**, *48*, 5337–5339. [[CrossRef](#)]
17. Zou, L.; Zhao, L.; Chen, P.; Guo, Y.-N.; Guo, Y.; Li, Y.-H.; Tang, J. Phenoxido and alkoxido-bridged dinuclear dysprosium complexes showing single-molecule magnet behaviour. *Dalton Trans.* **2012**, *41*, 2966–2971. [[CrossRef](#)]
18. Long, J.; Habib, F.; Lin, P.-H.; Korobkov, I.; Enright, G.; Ungur, L.; Wernsdorfer, W.; Chibotaru, L.F.; Murugesu, M. Single-Molecule Magnet Behavior for an Antiferromagnetically Superexchange-Coupled Dinuclear Dysprosium (III) Complex. *J. Am. Chem. Soc.* **2011**, *133*, 5319–5328. [[CrossRef](#)]
19. Shen, F.-X.; Pramanik, K.; Brandão, P.; Zhang, Y.-Q.; Jana, N.C.; Wang, X.-Y.; Panja, A. Macrocyclic supported dimetallic lanthanide complexes with slow magnetic relaxation in Dy₂ analogues. *Dalton Trans.* **2020**, *49*, 14169–14179. [[CrossRef](#)]
20. He, M.; Guo, F.-S.; Tang, J.; Mansikkamäki, A.; Layfield, R.A. Fulvalene as a platform for the synthesis of a dimetallic dysprosium single-molecule magnet. *Chem. Sci.* **2020**, *11*, 5745–5752. [[CrossRef](#)]
21. Aguilà, D.; Barrios, L.A.; Velasco, V.; Roubeau, O.; Repollés, A.; Alonso, P.J.; Sesé, J.; Teat, S.J.; Luis, F.; Aromí, G. Heterodimetallic [LnLn'] Lanthanide Complexes: Toward a Chemical Design of Two-Qubit Molecular Spin Quantum Gates. *J. Am. Chem. Soc.* **2014**, *136*, 14215–14222. [[CrossRef](#)]
22. Guo, Y.-N.; Chen, X.-H.; Xue, S.; Tang, J. Modulating Magnetic Dynamics of Three Dy₂ Complexes through Keto–Enol Tautomerism of the o-Vanillin Picolinoylhydrazone Ligand. *Inorg. Chem.* **2011**, *50*, 9705–9713. [[CrossRef](#)] [[PubMed](#)]
23. Cummins, C.C.; Schrock, R.R.; Davis, W.M. Synthesis of Terminal Vanadium (V) Imido, Oxo, Sulfido, Selenido, and Tellurido Complexes by Imido Group or Chalcogenide Atom Transfer to Trigonal Monopyramidal V[N₃N] (N₃N = [(Me₃SiNCH₂CH₂)₃N]³⁻). *Inorg. Chem.* **1994**, *33*, 1448–1457. [[CrossRef](#)]
24. Schrock, R.R.; Seidel, S.W.; Mösch-Zanetti, N.C.; Shih, K.-Y.; O'Donoghue, M.B.; Davis, W.M.; Reiff, W.M. Synthesis and Decomposition of Alkyl Complexes of Molybdenum (IV) That Contain a [(Me₃SiNCH₂CH₂)₃N]³⁻ Ligand. Direct Detection of α -Elimination Processes That Are More than Six Orders of Magnitude Faster than β -Elimination Processes. *J. Am. Chem. Soc.* **1997**, *119*, 11876–11893. [[CrossRef](#)]
25. Pinkowicz, D.; Birk, F.J.; Magott, M.; Schulte, K.; Dunbar, K.R. Systematic Study of Open-Shell Trigonal Pyramidal Transition-Metal Complexes with a Rigid-Ligand Scaffold. *Chem.—A Eur. J.* **2017**, *23*, 3548–3552. [[CrossRef](#)]
26. Brzozowska, M.; Handzlik, G.; Kurpiewska, K.; Zychowicz, M.; Pinkowicz, D. Pseudo-tetrahedral vs. pseudo-octahedral Er^{III} single molecule magnets and the disruptive role of coordinated TEMPO radical. *Inorg. Chem. Front.* **2021**, *8*, 2817–2828. [[CrossRef](#)]
27. Chilton, N.F.; Anderson, R.P.; Turner, L.D.; Soncini, A.; Murray, K.S. PHI: A powerful new program for the analysis of anisotropic monomeric and exchange-coupled polynuclear d- and f-block complexes. *J. Comput. Chem.* **2013**, *34*, 1164–1175. [[CrossRef](#)]
28. Liu, J.-L.; Chen, Y.-C.; Tong, M.-L. Symmetry strategies for high performance lanthanide-based single-molecule magnets. *Chem. Soc. Rev.* **2018**, *47*, 2431–2453. [[CrossRef](#)]
29. Guo, Y.-N.; Xu, G.-F.; Guo, Y.; Tang, J. Relaxation dynamics of dysprosium (iii) single molecule magnets. *Dalton Trans.* **2011**, *40*, 9953–9963. [[CrossRef](#)] [[PubMed](#)]
30. Liddle, S.T.; van Slageren, J. Improving f-element single molecule magnets. *Chem. Soc. Rev.* **2015**, *44*, 6655–6669. [[CrossRef](#)] [[PubMed](#)]
31. Aquilante, F.; Autschbach, J.; Carlson, R.K.; Chibotaru, L.F.; Delcey, M.G.; De Vico, L.; Fdez Galván, I.; Ferré, N.; Frutos, L.M.; Gagliardi, L.; et al. Molcas 8: New capabilities for multiconfigurational quantum chemical calculations across the periodic table. *J. Comput. Chem.* **2016**, *37*, 506–541. [[CrossRef](#)]
32. Sheldrick, G. Crystal structure refinement with SHELXL. *Acta Crystallogr. Sect. C* **2015**, *71*, 3–8. [[CrossRef](#)]
33. Arczyński, M.; Stanek, J.; Sieklucka, B.; Dunbar, K.R.; Pinkowicz, D. Site-Selective Photoswitching of Two Distinct Magnetic Chromophores in a Propeller-Like Molecule To Achieve Four Different Magnetic States. *J. Am. Chem. Soc.* **2019**, *141*, 19067–19077. [[CrossRef](#)] [[PubMed](#)]